Small

NANO · MICRO small
www.small-journal.com

RESEARCH ARTICLE OPEN ACCESS

Cryogenic TDS Platform for Quantitative Hydrogen Isotope ($H_2/D_2/HD$) Separation via Quantum Sieving in Porous Materials

Minji Jung[1] | Hyunlim Kim[1] | Michael Hirscher[2,3] | Hyunchul Oh[1,4]

[1]Department of Chemistry, Ulsan National Institute of Science and Technology (UNIST), Ulsan, Republic of Korea | [2]Max Planck Institute for Solid State Research, Stuttgart, Germany | [3]Advanced Institute for Materials Research (WPI-AIMR), Tohoku University, Sendai, Japan | [4]Graduate School of Carbon Neutrality, Ulsan National Institute of Science and Technology (UNIST), Ulsan, Republic of Korea

Correspondence: Michael Hirscher (m.hirscher@fkf.mpg.de) | Hyunchul Oh (hcoh@unist.ac.kr)

Received: 13 December 2025 | **Revised:** 13 April 2026 | **Accepted:** 27 April 2026

Keywords: cryogenic thermal desorption spectroscopy | hydrogen isotope | mass spectroscopy | porous materials | quantum sieving

ABSTRACT

Accurate evaluation of hydrogen isotope separation performance is critical for the development of advanced porous materials for energy, semiconductor, and nuclear applications. Herein, we report the development of an advanced cryogenic thermal desorption spectroscopy (AC-TDS) platform capable of quantitatively analyzing hydrogen isotopes (H_2, D_2, and even HD) over a wide temperature range (15 – 900 K). The system incorporates calibration standards such as TiH_2 and $Pd_{95}Ce_5$ alloy, enabling reliable quantification of desorbed gases. By varying the gas exposure temperature, time, and pressure, we can elucidate the microscopic nature of adsorption processes associated with structural flexibility, pore accessibility, or strong adsorption sites. With binary (H_2/D_2) and ternary ($H_2/HD/D_2$) isotope gas mixtures, AC-TDS directly determines isotope-dependent uptakes and selectivities using small quantities of samples and extracts desorption energetics via multi-rate analysis. Using specific gas exposure conditions, the TDS technique offers a powerful diagnostic tool for understanding adsorption energetics, framework dynamics, and isotope selectivity, and allows a rapid characterization of porous materials for hydrogen isotope separation applications based on selective adsorption.

1 | Introduction

The separation of hydrogen isotopes has become increasingly significant in both scientific and industrial domains, particularly as hydrogen plays a growing role in energy, semiconductor, and analytical technologies [1–3]. Deuterium (D_2), a stable isotope of hydrogen, is widely used in nuclear fusion research, neutron scattering [4, 5], semiconductor processing [6, 7], and life sciences [8, 9] due to its isotope effects [10–12]. However, the natural abundance of D_2 is extremely low (0.0156%) [13], necessitating efficient and scalable separation technologies to meet the rising demand. Among commercial options, cryogenic distillation (CD) is most commonly used for hydrogen-isotope separation, yet despite its maturity CD suffers from an inherently low separation factor (~1.5 at 25 K) and high energy consumption, limiting its suitability for compact or energy-efficient applications [14]. To overcome these limitations, attention has shifted toward quantum sieving (QS) in nanoporous materials. QS exploits the quantum mechanical nature of light gases (e.g., H_2, He) at cryogenic temperatures and is typically categorized into kinetic quantum sieving (KQS), where heavier isotopes diffuse more effectively through sub-nanometer pores, and chemical affinity quantum sieving (CAQS), which arises from zero-point-energy differences that lead to preferential adsorption of heavier isotopes.

Various nanoporous materials such as metal–organic frameworks (MOFs), nanoporous carbons, and porous polymers have shown promising QS-based selectivity for hydrogen isotopes [15–21].

To fully harness this potential, precise and quantitative methods are essential for evaluating performance under cryogenic conditions. Common approaches include the ideal adsorbed solution theory (IAST), breakthrough experiments, and gas chromatography (GC). Each has notable limitations: IAST predicts selectivity from single-component isotherms [22], but its ideal-solution assumption can deviate from experiment in systems with sorption hysteresis (e.g., flexible or diffusion-limited MOFs) [23], Breakthrough experiments directly probe binary or ternary separations under dynamic flow [24], but typically require gram-scale adsorbent (which is not suitable for novel samples) and provide limited insight into adsorption sites and structural origins. GC can probe hydrogen-isotope mixtures [25, 26], yet its inherently discontinuous pulse injection hampers capture of transient, KQS-relevant dynamics, and column customization is nontrivial. These constraints highlight the need for a practical, precise, and versatile technique that can quantitatively assess adsorption and separation under QS regimes.

On the other hand, thermal desorption spectroscopy (TDS) provides a practical tool to probe gas–solid interactions with minimal sample quantities, allowing for direct isotope quantification via a quadrupole mass spectrometer (QMS) [27–31]. Historically, TDS was developed for (chemisorbed) surface studies at above room temperature and later extended to cryogenic operation, enabling physisorbed surface observations relevant to quantum sieving; subsequent reports adapted TDS specifically for hydrogen-isotope separation. Fortunately, hydrogen provides a crucial exception to this constraint, unlike inert gases, it forms reversible hydrogen–metal interactions, so one can use standard hydrides (e.g., TiH_2) or hydrogen-absorbing metals (e.g., Pd–Ce alloy) [32] pre-loaded with known amounts of H_2, D_2, or HD. The following thermal desorption run allows to determine absolute quantities from the desorbed gas. However, precise quantification still demands high-temperature calibration because TiH_2 and Pd-based standards release hydrogen isotopes only at elevated temperatures (~400 K for Pd–Ce and ~740 K for TiH_2). This creates a fundamental challenge for cryogenic TDS systems that must observe physisorption and isotope-selective uptake at cryogenic temperatures but protect ultra-low-temperature components such as sample holders, detector interfaces, and seals that can degrade above ~300 K. Thus, a TDS platform that seamlessly accommodates both cryogenic measurement and high-temperature calibration requires careful thermal management to safeguard sensitive components. Prior systems have realized low temperatures utilizing a liquid-helium cryostat operating down to ~20 K [33, 34], but these can only operate cost-efficiently if a low-temperature facility with recovery and liquefaction is in-house available. Typically, these cryostats do not allow high-temperature calibration within the same instrument; to our knowledge, no existing TDS system has provided full-range analysis from 15 to 900 K while enabling both quantitative calibration and isotope-selectivity measurements under cryogenic conditions. (Table S1) In particular, quantitative analysis of HD together with H_2 and D_2 is important because HD inevitably forms in hydrogen isotope mixtures through isotope scrambling. However, previous cryogenic TDS studies have primarily focused on binary isotope analysis and have not demonstrated quantitative HD detection. Here, we demonstrate that TDS can be used for the quantitative analysis of H_2, HD, and D_2.

While cryogenic TDS for hydrogen adsorption/desorption has been reported previously [33, 34], the novelty of the present work lies in the development of a quantitatively calibrated AC-TDS platform that combines 15–900 K operation, high-temperature calibration, and direct quantification of H_2, D_2, and HD within a single instrument. This broader temperature window is particularly important for hybrid hydrogen-storage materials that contain both cryogenic physisorption and high-temperature chemically bound hydrogen release, such as porous $Mg(BH_4)_2$ [35], because both contributions can be distinguished on the same sample. In addition, by using TiH_2 and $Pd_{95}Ce_5$ calibration standards together with controlled H/D scrambling, the present platform enables quantitative H_2/HD/D_2 analysis under realistic mixed-isotope conditions, including HD, which has not been reliably addressed in earlier cryogenic TDS publications. More importantly, AC-TDS goes beyond simple desorption measurement by helping to explain why a material behaves as it does: it can relate isotope selectivity to adsorption energetics and can also show whether low cryogenic uptake comes from intrinsically weak adsorption or from pores that were not fully open or accessible before thermal activation, as described by thermally responsive porous frameworks such as ZIF-7 [36]. Additionally, for zeolites with open Cu^+ centers, activation temperatures above 500 K are required to remove residual oxygen or water species, and this can now be achieved within the same setup without breaking vacuum conditions [37]. Thus, the method provides a unified way to analyze adsorption strength, pore accessibility, and framework response within one experimental platform.

2 | Experimental Setup and Measurement Procedures

2.1 | Set up for TDS

Figure 1(a) and Figure S1 shows a schematic diagram of the home-built advanced cryogenic thermal desorption spectroscopy (AC-TDS) system, which is capable of measuring at both cryogenic and high-temperature conditions. Turbo molecular pumps (1), (10) were installed to achieve a high vacuum condition (~10^{-8} mbar) in the sample chamber and quadrupole mass spectrometer (QMS) chamber, respectively. The sample holder (2) and heater (3) were made of oxygen-free conductivity copper material for efficient heat transfer. Therefore, the heater allows the sample to be heated up to 900 K. The sensors for measuring the temperature of the sample were configured with a thermocouple sensor (4) for high temperatures and a diode sensor (5) for cryogenic temperatures. The diode sensor can be detached from the sample holder before high-temperature measurements, thereby preventing exposure to elevated temperatures. The cryocooler system (6) can cool the sample down to 15 K. A bellows system (7) was introduced for measurements from 15 to 900 K. The gases are injected into the sample chamber via the gas inlet part (8), and the gas desorbed from the sample is analyzed through a quadrupole mass spectrometer (9), which detects a mass range of 1–200 amu. The bellows system in the AC-TDS enables sample analysis under both cryogenic and

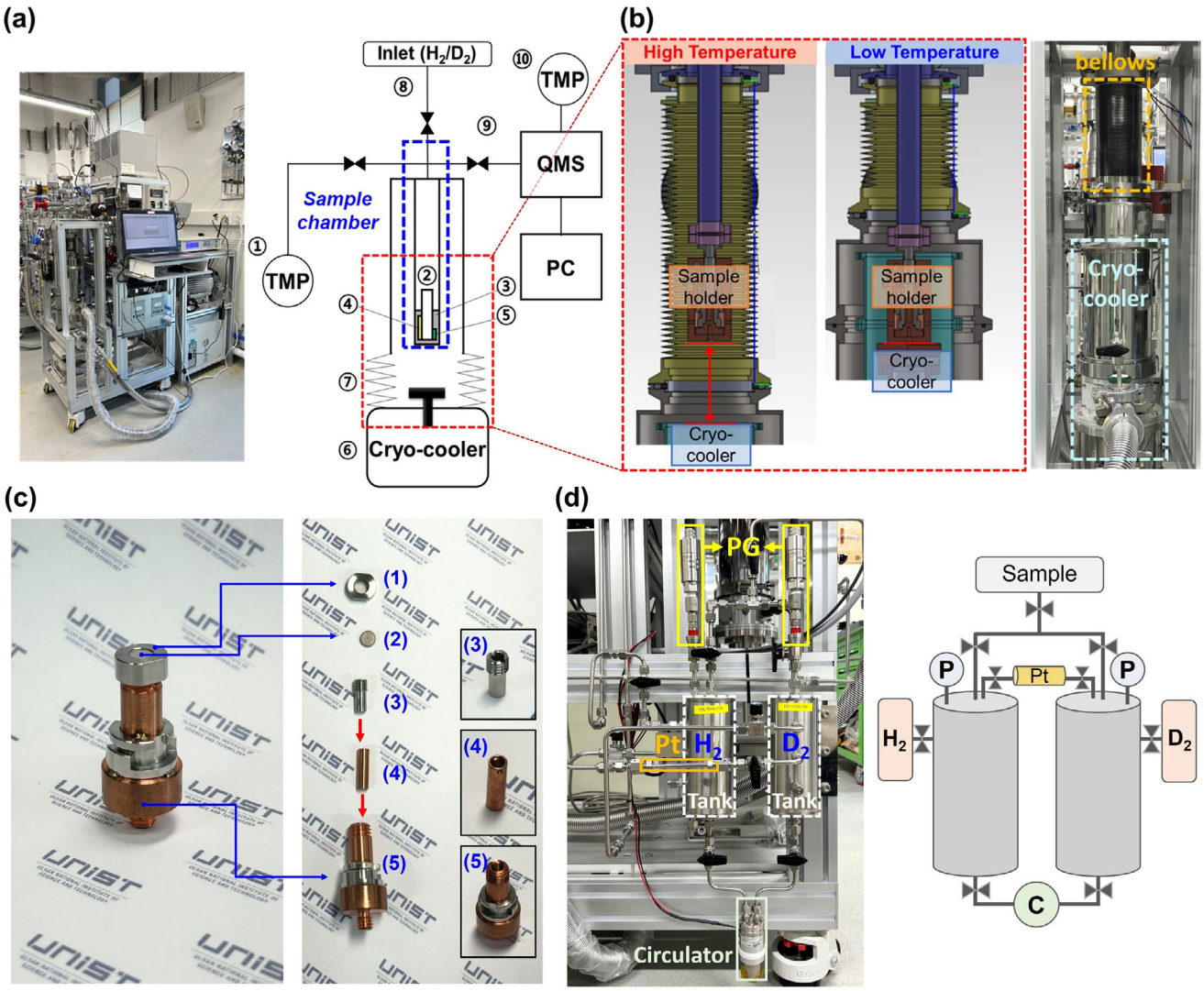

FIGURE 1 | (a) The schematic diagram of Advanced-cryogenic thermal desorption spectroscopy (AC-TDS). The indexed parts are: turbo molecular pump (1),(10), sample holder (2), heater (3), thermocouple sensor (4), diode sensor (5), cryo-cooler (6), flexible vacuum bellows system (7), gas inlet part (8), quadrupole mass spectrometer (9). Vacuum bellows system (b) The up and down bellows system in cryogenic and high-temperature conditions, respectively, and the photo of the bellows system. (c) The sample holder (5) with a stainless cap (1), gasket (2), screw part (3), and copper sample cell (4). (d) The photo (left) and the schematic diagram (right) of the H_2-D_2 mixture tank.

high-temperature conditions. Figure 1(b) shows the sample holder and the position of the cryo-cooler at low and high temperatures, respectively. For high-temperature measurements, the position of the cryocooler can be lowered, resulting in physical separation from the sample holder and thereby protecting it from heat exposure. In contrast, during measurements for cryogenic conditions, the sample holder remains in complete contact with the cryo-cooler, allowing it to be maintained at cryogenic temperatures. As a result, AC-TDS can be measured across a wide temperature range using a flexible bellows system, which adjusts in length according to experimental conditions. Furthermore, validation with TiH_2 confirmed that AC-TDS ensures precise temperature control and a constant heating rate, thereby enabling reliable desorption analysis. (Figure S2) To demonstrate the accuracy and reliability of the AC-TDS with respect to variations in heating rate, calibration constants were measured across a range of heating rates from 3 to 7 K min^{-1}. The calibration constants obtained at different ramping rates were plotted as a scatter plot, with the dashed line indicating the average value. The calibration constants remained consistent within experimental error at all heating rates (Figure S3), confirming the suitability of AC-TDS for accurate analysis under varying ramping conditions.

The sample holder (5) is constructed from copper and stainless steel and features a screw beneath the holder that allows it to be securely fixed to the bottom of the sample chamber. (Figure 1(c)) When loading and removing a sample into the holder, the sample holder must be assembled in the following order: (4) copper sample cell—(3) screw—(2) gasket—(1) cap. The size of the copper sample cell is 14 mm in height and 2.8 mm in diameter. The powder or solid sample can be loaded into the copper sample cell. The screw should be used to prevent the copper sample cell from being lifted by the vacuum conditions. Next, the gasket must be placed on top of the screw to avoid powder samples from being blown out due to gas injection or evacuation.

2.2 | Preparation of Deuterium Hydride HD

Hydrogen isotope mixtures containing H_2, HD, and D_2 are frequently encountered in both fusion and semiconductor technologies. In these applications, even trace amounts of HD can compromise the required isotopic purity of D_2, making its selective removal essential. Accordingly, accurate quantification of HD is critical for evaluating separation performance. To facilitate such analysis, a controlled HD generation system was constructed based on the equilibrium reaction of an H_2/D_2 mixture in the presence of a platinum (Pt) catalyst (Equation (1)).

$$H_2 + D_2 \overset{Pt}{\leftrightarrow} 2HD \tag{1}$$

An equimolar mixture of hydrogen and deuterium was reacted using a Pt catalyst (platinum on alumina, pellets, 3.2 mm, Sigma–Aldrich), and the HD generation system is shown in Figure 1(d). H_2 and D_2 gases are individually filled into separate tanks of equal volume at the same pressure, and the pressure of each gas can be monitored using each pressure gauge. Both tanks are connected to a gas circulator (Thomas GK M-02), with the bottom of one tank connected to the input valve and the bottom of the other tank connected to the output valve. Furthermore, each tank is connected to both ends of the Pt catalyst column, with valves placed between the tanks and the column. Afterward, the Pt catalyst valve of each tank is opened, allowing the mixture to react with the Pt catalyst. Simultaneously, the gas circulator valves are opened, allowing continuous circulation of the gases through the circulator. A H_2-D_2 catalytically-induced scrambling reaction occurs at room temperature and creates HD molecules until the equilibrium concentration $H_2/HD/D_2$ of 1:2:1 is reached after some time. Finally, this hydrogen isotope mixture can flow into the sample chamber and be adsorbed by the sample.

Increasing the reaction time with the Pt catalyst through the gas circulator, i.e., H–D scrambling, enhances the HD content. To determine the reaction time required to reach equilibrium, commercial activated carbon, MSC-30, was exposed at 25 K and 1 bar for 3 min to gas mixtures generated after different reaction times, and the corresponding TDS spectra were recorded. The subsequent desorption spectra of H_2, HD, and D_2 are shown in Figure 2. After 1 min of reaction, HD was not detected (Figure 2a). HD appeared by 10 min (Figure 2b) and continued to increase with further reaction, reaching a time-invariant spectrum by ~60 min (Figure 2c,d). Furthermore, to examine whether the gas circulator induced excessive HD formation, the system was kept quiescent (no circulation) for 24 h after the 60 min reaction. If overproduced HD were present, it would have gradually returned to equilibrium during this quiescent period. The TDS spectrum was essentially unchanged from the 60 min case (Figure 2e), indicating that equilibrium had already been reached during circulation. Throughout these experiments the total desorption peak area remained constant (Figure 2f), confirming that the overall uptake is constant and that only the relative abundances of H_2, HD, and D_2 evolved due to isotopic exchange. At ambient conditions, statistical scrambling of H_2 and D_2 in the presence of a catalyst is expected to yield an $H_2/HD/D_2$ ratio of 1:2:1. While our spectra do not directly quantify these absolute fractions, since the porous material additionally imposes quantum sieving effects, which increase the adsorbed amount for heavier isotopes. Nevertheless, the observed time-invariance after ~60 min is consistent with a near-equilibrated isotope mixture of 1:2:1 in the gas. Accordingly, we adopt ~60 min reaction/exchange time to ensure a stable gas mixture.

2.3 | Quantitative MS Calibration for H_2, D_2, and HD

The quadrupole mass spectrometer (QMS) reads the partial pressure of the desorbing species during constant evacuation by a turbo-molecular pump. For calibration, a known amount of gas has to be introduced into the vacuum without giving rise to a strong pressure increase beyond the linear and operational range of the QMS. For hydrogen, hydrogen-containing metals or metal hydrides offer a unique opportunity to introduce well-defined, small amounts of hydrogen gas. We used two references, a classical hydride TiH_2 (Titanium (II) hydride, 99%, 325 mesh powder, Alfa Aesar) and a hydrogen-absorbing palladium cerium ($Pd_{95}Ce_5$) alloy, to cover a wide temperature range. TiH_2 contains 4 wt.% of hydrogen and decomposes at elevated temperatures releasing hydrogen and therefore is often used as a standard for H_2 quantification. Owing to the high hydrogen content, typically only small amounts of TiH_2 in the range of milligrams are needed, thus avoiding a saturation of the QMS at typical heating rates.

For hydrogen isotopes, a palladium cerium alloy ($Pd_{95}Ce_5$ alloy) was used for TDS calibration. In dilute Pd-rare-earth metal (RE) alloys, RE (Y, Ce, Gd) is substitutionally included in the fcc lattice of Pd. During moderate hydrogen loading and avoiding the formation of the β hydride phase in Pd, H_2, or D_2 dissociates on the Pd surface, diffuses in the matrix, and forms Pd–RE–H(D) complexes. The reorientation of this complex gives rise to characteristic relaxation maxima in internal friction measurements [38–40]. Owing to the trapping at the RE, the hydrogen-loaded samples can be handled at ambient conditions. The $Pd_{95}Ce_5$ alloy can be loaded with H_2 or D_2 by forming a stable Pd–Ce–H(D) complex. The maximum hydrogen content is reached if each Ce atom traps one hydrogen atom, i.e. in our case at 5 at% hydrogen. This relatively low hydrogen content compared to TiH_2, requires the use of larger sample masses, typically 100 mg to 1 g. The hydrogen content of the $Pd_{95}Ce_5H_x$ samples can be determined by weighing before and after the TDS measurements, denoting the mass difference to the desorbed amount of H_2.

Prior to use, $Pd_{95}Ce_5$ was etched in aqua regia (HNO_3 + 3HCl) to remove surface oxides, then annealed at 840 K under UHV to eliminate any hydrogen introduced during etching. The alloy was weighed, hydrogenated in H_2/D_2 at 353 K for 2 h at controlled pressures (50, 100, 120, or 200 mbar), quenched to cryogenic temperature in liquid N_2, and returned to room temperature for re-weighing on a microgram balance. The mass gain gives the absolute uptake of H_2 and D_2 stored in the alloy. For TDS, the alloy was subsequently heated to 840 K at 6 K min^{-1}. The hydrogen content of TiH_2 was determined stoichiometrically from its formula and the measured sample mass.

Because the QMS is coupled to a turbomolecular pump operating at constant pumping speed, the QMS signal I(t) is proportional to

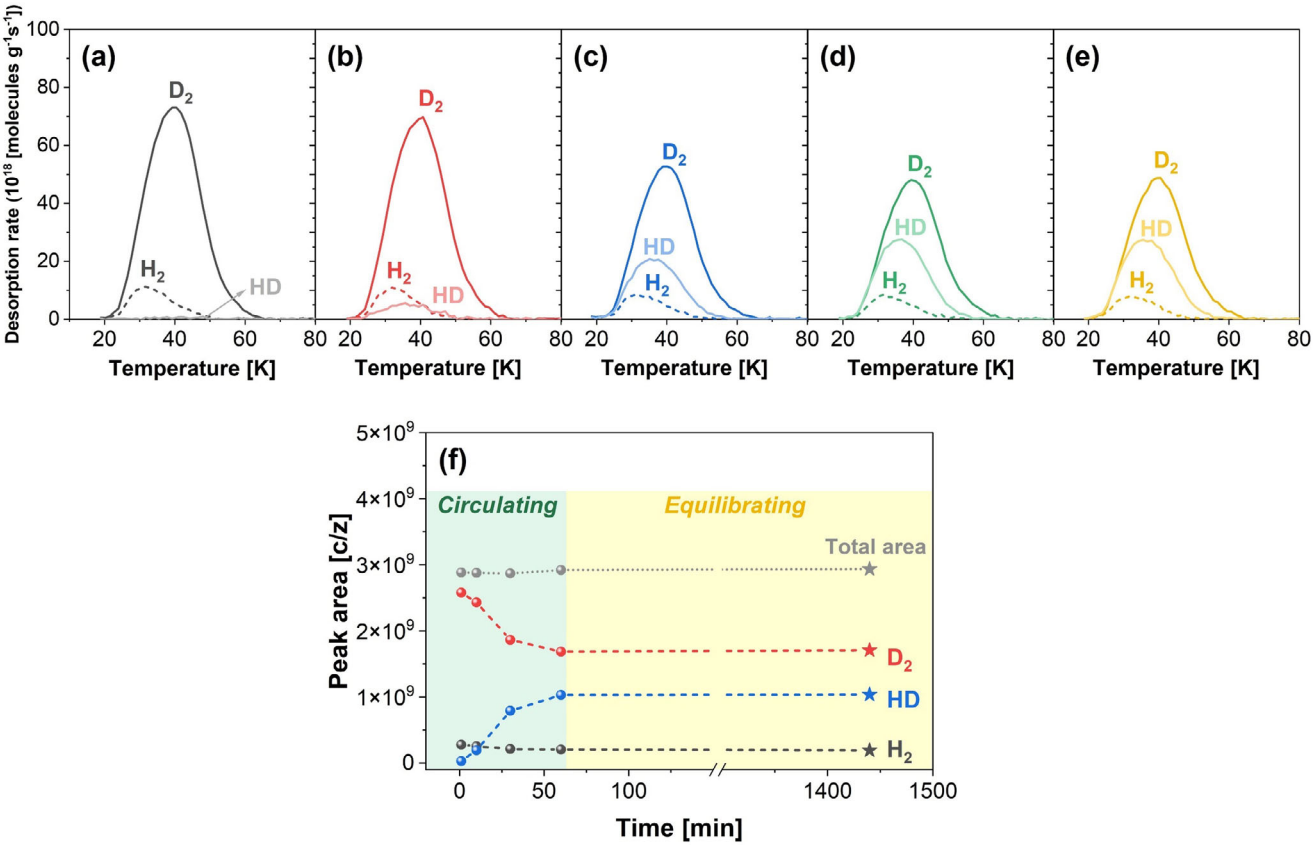

FIGURE 2 | TDS spectrum of H_2, D_2, and HD in MSC-30 using HD mixture at various reaction times of (a) 1, (b) 10, (c) 30, (d) 60 min, and (e) after equilibrating for 24 h without circulating. (f) The peak area of H_2, HD, D_2, and the total area correspond to the circulating and equilibrating times. Circle symbols: circulating times; star symbol: equilibrating times.

the instantaneous desorption rate [32].

$$3\ \mathrm{I}\ (\mathrm{t}) = \alpha \frac{dn(t)}{dt} \tag{2}$$

where α is the proportionality constant and $n(t)$ is the number of molecules desorbed from the samples at the time t. The integral in the range of the start time t_0 and final time t_1 of Equation (3) is given by:

$$\int_{t_0}^{t_1} I(t)\,dt = \alpha \int_{t_0}^{t_1} \frac{dn(t)}{dt} dt \tag{3}$$

Equation (3) means that the number of desorbed molecules is proportional to the area under the desorption curve. The proportional constant α can be obtained through the desorption spectrum by measuring a known amount of hydrogen isotope gases.

Figure 3 and Figure S4 summarize the calibration behavior of the two standards. For TiH_2, H_2 is released in a single, sharp event: the TDS peak appears within a narrow 40 K window (750~790 K) and is essentially complete by ~790 K (Figure 3a), consistent with rapid atomic decomposition. In contrast, D_2 stored in $Pd_{95}Ce_5$ desorbs gradually over a broad range (400~700 K; Figure 3c), as expected for detrapping from Ce and diffusion. In both cases, the time-integrated QMS signal (area under the curve, $A = \int I\,dt$) scales linearly with the amount released: A_{H2} vs TiH_2 mass (Figure 3b, $R^2 = 0.999$) and A_{D2} vs desorbed D_2 mass from $Pd_{95}Ce_5$ (Figure 3d, $R^2 = 0.998$). These linear relationships establish TiH_2 and $Pd_{95}Ce_5$ as quantitative calibrants over their respective temperature windows. HD calibration was established within the same $Pd_{95}Ce_5$-based protocol by combining m/z-resolved TDS analysis with mass-balance determination in ternary H_2/HD/D_2 exposures. (Figure 3e) Any other contribution to m/z = 3 can be excluded due to the low natural occurrence of ^{3}He and T or T_2.

For HD calibration, the alloy was exposed to an H_2/HD/D_2 mixture, and the total uptake was determined from the sample mass before and after exposure. The H_2 and D_2 contributions were quantified from their integrated TDS areas using the corresponding calibration constants, and the remaining mass, i.e., the difference between the total absorbed mass and the sum of the calibrated H_2 and D_2 masses, was assigned to HD (Figure S5). Correlation of this HD mass with the integrated m/z = 3 area yielded a linear area–mass relationship (Figure 3f, $R^2 = 0.998$), thereby establishing quantification of HD together with H_2 and D_2 [41].

2.4 | Measurement Protocol

Pure gas room-temperature exposure (Figure 4a). To probe physisorption with minimal kinetic bias, the sample is first exposed to a pure isotope (H_2 or D_2) at room temperature (RT), then cooled to 18 K. Residual gas in the manifold is removed by

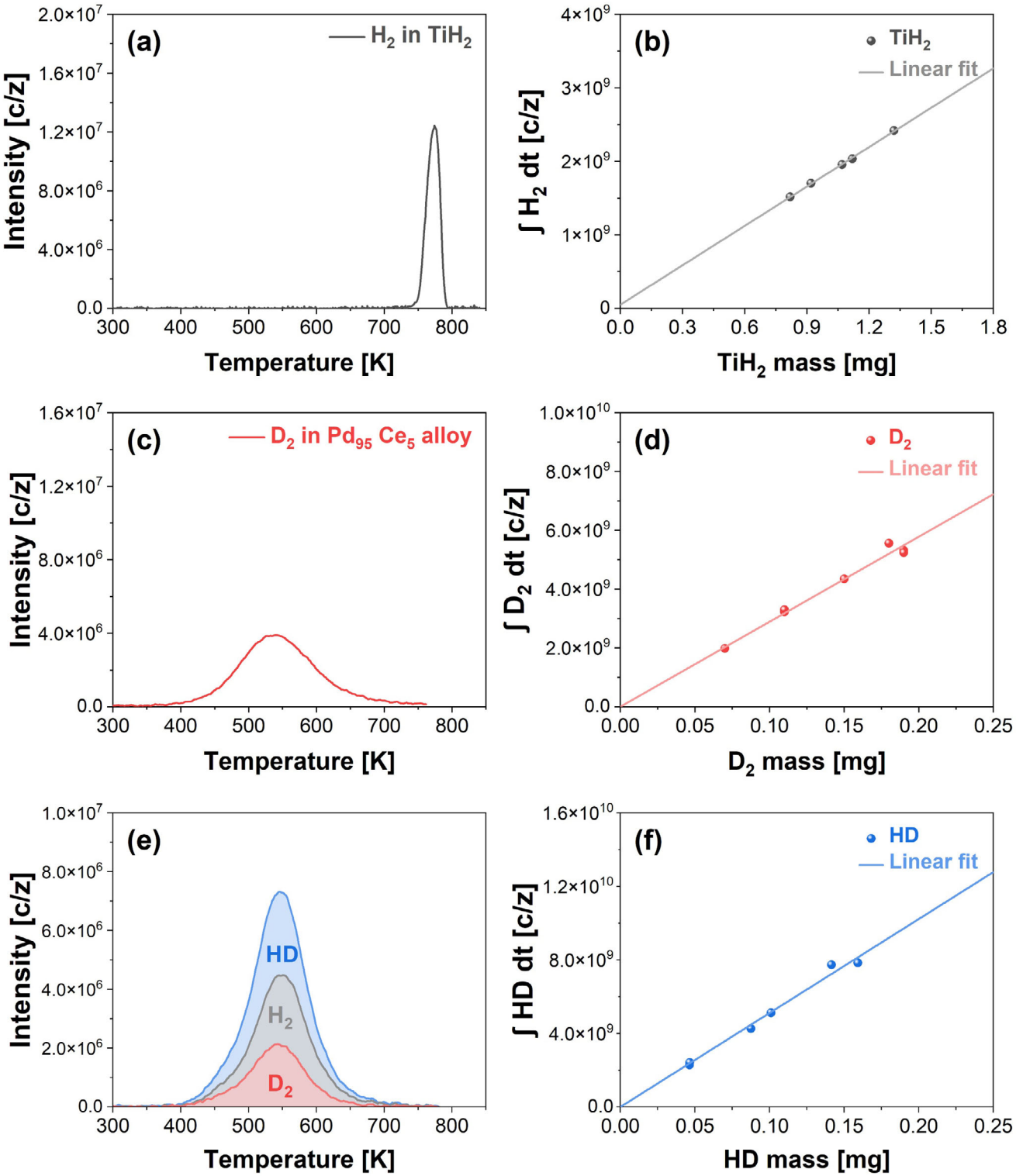

FIGURE 3 | TDS spectra of (a) H_2, (c) D_2, and (e) HD in calibration standards (TiH_2, $Pd_{95}Ce_5$ alloy). The correlation of weight and the area under the desorption curves for (b) H_2, (d) D_2, and (f) HD.

evacuation to ~10^{-5} mbar, after which the sample is heated at a constant rate while QMS records the desorbing species.

Pure gas liquefaction-temperature exposure (Figure 4b). Alternatively, the sample is cooled to the liquefaction temperature (20 K for H_2, 23 K for D_2) before gas exposure. After a defined exposure/hold, the manifold is evacuated (~10^{-5} mbar), the sample is set to 18 K, and a constant-rate temperature ramp is applied for TDS.

Diagnostic use of the two protocols (Figure 4d,e). These paired protocols distinguish rigid from flexible frameworks. In rigid, open-pore materials (e.g., MSC-30), the uptake and ensuing TDS profile are essentially independent of dosing temperature

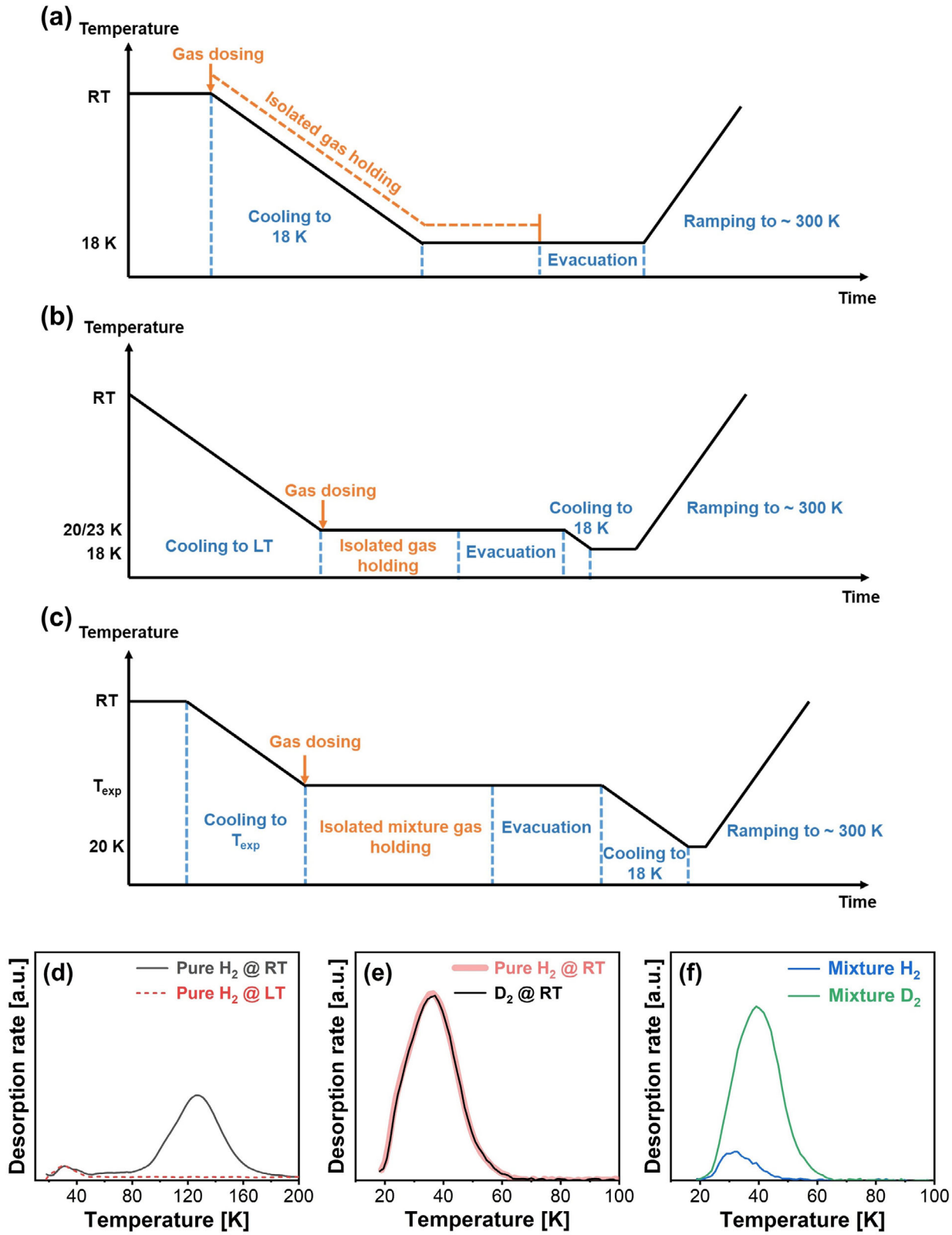

FIGURE 4 | The procedure of TDS measurement for pure gas loaded at (a) room temperature and (b) liquefaction temperature. (c) The procedure of TDS measurement for a binary or ternary mixture. (d) The TDS spectrum of pure H_2 in Cu-ZIF-gis with a rigid structure. (e) The TDS spectrum of pure H_2 in MSC-30 with local flexibility. (f) The TDS spectrum of H_2/D_2 1:1 mixture in MSC-30 at 25 K.

(Figure 4e), indicating no gating or thermally driven transitions. In locally flexible frameworks (e.g., Cu-ZIF-gis), room-temperature dosing can admit molecules via breathing/gate opening, yielding a clear desorption signal on heating, whereas gas exposure near 20–23 K kinetically excludes entry and produces little or no signal (Figure 4d). The contrast provides a sensitive, experiment-internal probe of temperature-dependent structural dynamics and adsorption accessibility.

Binary/ternary mixtures (Figure 4c,f). For isotope separation tests, an H_2/D_2 (or $H_2/HD/D_2$) mixture is exposed at a chosen T_{exp} , the manifold is evacuated, the sample is cooled to 18 K, and TDS is performed at a fixed ramp rate. (Figure 4c) Representative spectra for an H_2/D_2 (1:1) feed at 25 K are shown in Figure 4f. The uptake of each isotopologue is obtained by integrating the corresponding desorption peak area, and selectivity is reported as the ratio of integrated uptakes (*e.g.*, $S_{D2/H2} = nD_2/nH_2$). This protocol enables direct, temperature-resolved comparison of adsorption and isotopic preference, linking observed behavior to pore accessibility, framework dynamics, and quantum-sieving effects.

3 | Low to High-Temperature Case Study and Quantum-Sieving Analysis

3.1 | Investigation of the Catalyst on Porous Support

The AC-TDS platform resolves physisorption at cryogenic temperatures and chemisorption at elevated temperatures within a single run, which is critical for screening hydrogen-storage/production catalysts. As a case study, Ru catalysts on porous Al_2O_3 and MgO were loaded with pure D_2 gas at 1 bar and room temperature, then analyzed under a 6 K min^{-1} ramp (Figure 5a) [42]. Both samples released the cryogenically held D_2 completely near 70 K, giving comparable low-temperature single gas uptakes (Ru/Al_2O_3: 3.81 mmol g^{-1}; Ru/MgO: 2.36 mmol g^{-1}), consistent with physisorption governed largely by accessible surface area. In contrast, the high-temperature portions of the spectra diverge: Ru/Al_2O_3 shows a desorption maximum around 310 K, whereas Ru/MgO desorbs later, centered near 380 K. The temperature shift indicates stronger chemisorptive binding on Ru/MgO than on Ru/Al_2O_3. Thus, AC-TDS readily separates weak, low-temperature adsorption from stronger, catalytically relevant chemisorption and provides a direct, comparative measure of binding strength within one experiment.

3.2 | Binding Energy and Pore Size Dependent Desorption Behavior

The TDS spectra exhibit characteristic variations as a function of binding energy and pore size, allowing direct comparison of desorption behaviors governed by adsorption strength and confinement. At low temperature, the desorption peak position reflects confinement and site strength: smaller pores and stronger sites shift peaks to higher temperatures (schematic, Figure 5b). We first benchmarked MOF-74(Ni)-IM, which presents a high density of open metal sites (OMSs) (Figure 5c) [43]. Three features are resolved: (i) ~35 K, weak interactions on the aromatic benzene ring; (ii) ~50 K, adsorption near triangular Oxygen; (iii) ~90 K, strongest binding at Ni OMSs. These assignments, consistent with diffraction-derived site maps, illustrate how AC-TDS deconvolves adsorption sites by energetics. Pore geometry effects were then compared across frameworks with distinct apertures (Figure 5d). MOF-5 (large pores, ~12–15 Å) exhibits low-temperature peaks (~20 and ~40 K) characteristic of weak van der Waals binding [44]. MOF-303 (smaller channels; ~6 Å along *a*, 3.2–3.9 Å along *c*) shifts features upward (~30 and ~50 K), evidencing stronger confinement [17]. FMOF-Cu, which lacks OMSs but possesses three cavity types connected by narrow windows (3.6/2.5 Å), shows a ~55 K peak from adsorption in the cavities and a higher-temperature feature near 100 K attributable to gate-opening/restricted diffusion, not to strong chemisorption [21]. Collectively, these datasets demonstrate that AC-TDS sensitively maps site energetics, pore-size effects, and framework dynamics (e.g., gating), providing a quantitative basis for understanding cryogenic hydrogen-isotope uptake and separations.

3.3 | Evaluation of Isotope Mixture Selectivity Based on Quantum Sieving in MSC-30

MSC-30 (Kansai Coke and Chemicals Co., Ltd.) with a high porosity and a BET area of 3019 m^2g^{-1} was conducted using a binary (H_2/D_2) equimolar mixture under 1 bar and various exposure temperatures (25, 30, and 40 K) conditions (Figure 5e). Maximum isotope uptake was observed at 25 K, and the total uptake decreased with increasing temperature, consistent with thermal deactivation of the adsorption. Moreover, at all temperatures, D_2 exhibited higher uptake, consistent with the KQS effect, in which heavier isotopes are preferentially adsorbed in confined nanopores due to their shorter de Broglie wavelengths and lower zero-point energies. During the measurement, no signal of HD was observed, indicating that the exchange process did not occur without a (Pt) catalyst during H_2/D_2 mixing.

The separation selectivity for D_2 over H_2 was quantified based on TDS peak areas, calibrated using standard response factors for each gas. Selectivity is defined as the ratio of the molar fraction in the adsorbed phase(x) to that in the gas phase(y) as shown in (Equation 4);

$$Selectivity = \frac{x(D_2)/x(H_2)}{y(D_2)/y(H_2)} \tag{4}$$

However, because the volume of the TDS sample chamber greatly exceeds the amount of gas adsorbed, the change in gas-phase composition during loading is negligible. Thus, selectivity can be simplified as:

$$Selectivity = \frac{Area(D_2)\cdot C(D_2)}{Area(H_2)\cdot C(H_2)} \tag{5}$$

where Area(D_2) and Area(H_2) represent the under area of desorption for each gas, and C(D_2) and C(H_2) are the calibration constants of each gas.

The D_2/H_2 selectivity values determined using a binary mixture at each temperature are shown in Figure 5f. MSC-30 exhibits a maximum selectivity of 8.2 at 25 K, which decreases with

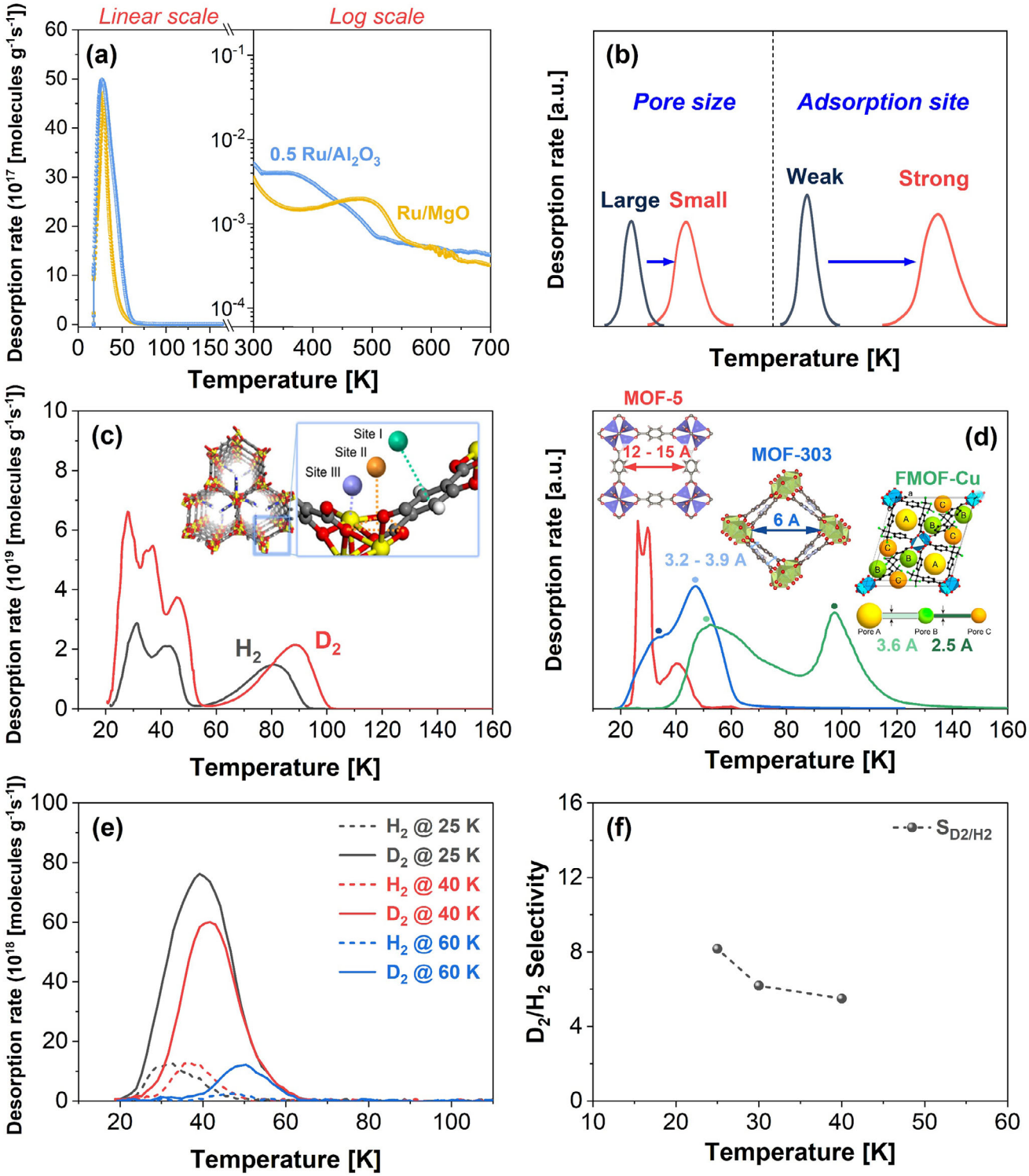

FIGURE 5 | (a) TDS spectrum of D_2 in Ru/Al_2O_3 and Ru/MgO catalysts from cryogenic to high temperature conditions [42]. (b) Schematic diagram of changes in desorption temperature based on pore size and adsorption site. (c) TDS spectrum for pure H_2 and D_2 in MOF-74(Ni)-IM with open metal site (OMS) [39]. (d) TDS spectrum for pure H_2 in different nanoporous materials with various pore sizes. (MOF-5 [44], MOF-303 [17] and FMOF-Cu [21]) (e) TDS spectra of 1 bar binary (H_2/D_2) and ternary ($H_2/HD/D_2$) mixture on MSC-30 at 25 K (f) D_2/H_2 selectivity and D_2/HD selectivity after exposure to binary and ternary mixtures in MSC-30.

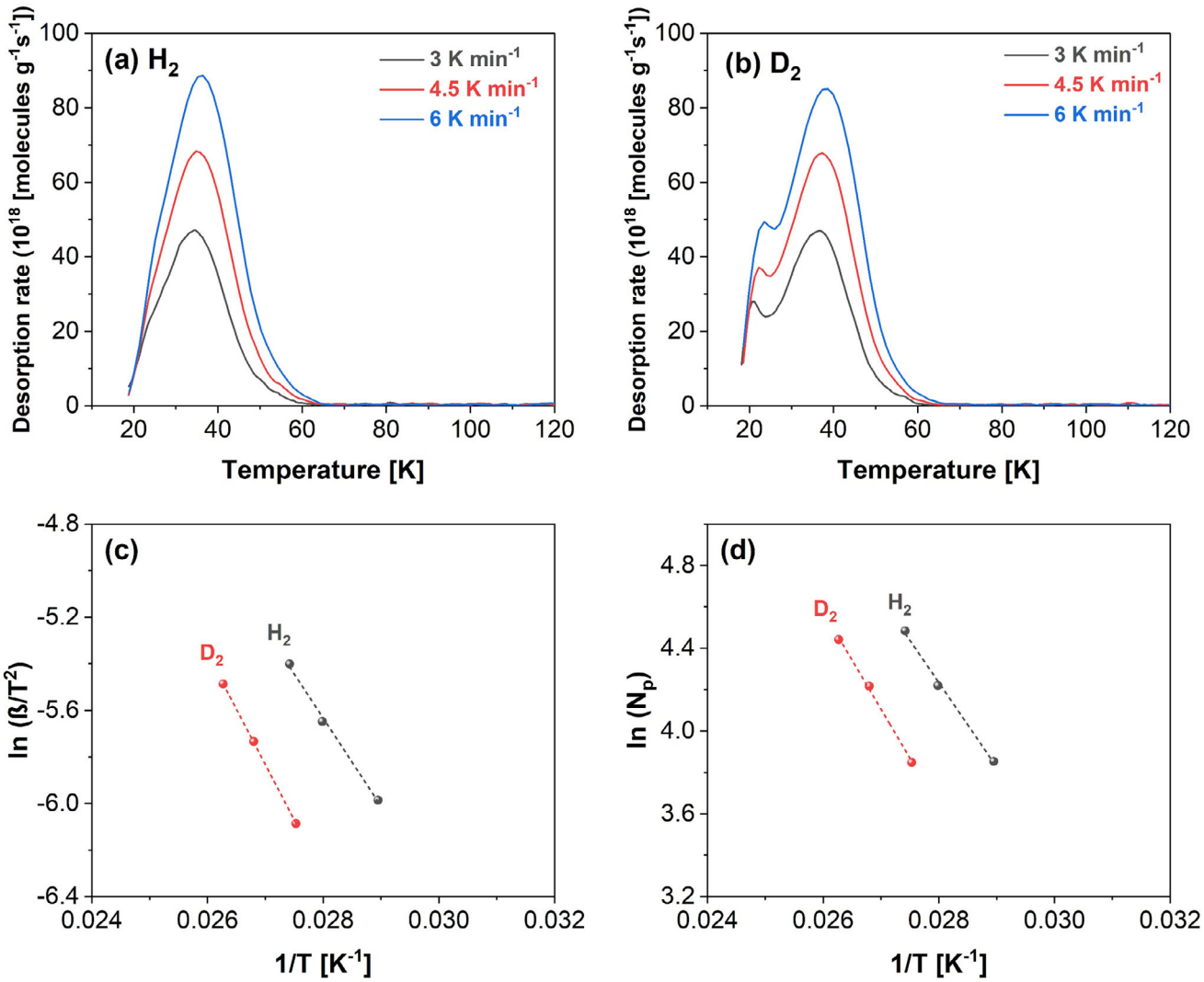

FIGURE 6 | TDS spectrum of pure (a) H_2 and (b) D_2 at RT with a heating rate of 3, 4.5, and 6 K min^{-1} in MSC-30, the desorption rate plot by using the heating rate (c), and the desorption rate (d).

increasing temperature. This trend is attributed to the KQS effect, in which quantum size exclusion more strongly affects lighter isotopes (e.g., H_2), thereby enhancing D_2 selectivity at cryogenic temperatures.

For a ternary mixture, prior to dosing, the gas mixture was equilibrated by circulating it in a mixing tank for 1 h to ensure homogeneous composition. TDS spectra for all three isotopes are shown in Figure S6. The results clearly reveal isotope-dependent desorption behavior. Among the three species, D_2 exhibited the highest adsorption, followed by HD, while H_2 showed the lowest uptake. MSC-30 exhibited $S_{D2/H2}$ and $S_{D2/HD}$ selectivities of 7.4 and 2.2, respectively, at 25 K.

4 | Desorption Energetics

In addition to selectivity, desorption energy provides valuable information on the strength of isotope–surface interactions. The desorption energy (E_{des}) can be derived from TDS spectra obtained at different heating rates using the Polanyi–Wigner equation. (Equation 6) [45]. This equation assumes that the desorption peak maxima correspond to the desorption rate and fractional surface coverage at desorption peak maxima is independent of the heating rate.

$$-\frac{d\theta}{dt} = \nu \cdot \exp\left(-\frac{E_{des}}{RT}\right) \cdot \theta \tag{6}$$

where θ is coverage, ν is a preexponential factor, Edes is desorption energy, R is the ideal gas constant, and T is temperature. In the TDS system, the measurement proceeds with a linear heating rate, the temperature can be described as follows

$$T = T_0 + \beta \cdot t \tag{7}$$

where T_0 is the initial temperature, β is the heating rate, and t is time since the start of the spectrum. As a result, the Polanyi–Wigner equation can be rewritten as

$$\ln\left(\frac{\beta}{T_{max}^2}\right) - \frac{E_{des}}{RT_{max}} + \ln\left(\frac{\upsilon R\theta_0}{E_{des}}\right) \tag{8}$$

Desorption energy can be calculated using the slope obtained by plotting $\ln(\beta/T^2_{max})$ vs. $1/T_{max}$. As an alternative equation to calculate the desorption energy, Falconer proposed an equation that uses the maximum desorption rate, excluding the value of the heating rate [46].

$$\ln\left(N_p\right) = -\frac{E_{des}}{RT_{max}} + \ln\left(\upsilon \cdot \theta\right) \quad (9)$$

where N_p is the maximum desorption rate (amplitude of desorption curve). The slope obtained by plotting $\ln(N_p)$ vs. $1/T_{max}$, and the desorption energy can be calculated from the slope.

Figure 6a,b shows the TDS spectra of pure H_2 and D_2 in MSC-30 at room temperature under various heating rates of 3, 4.5, and 6 K min^{-1}. The maximum desorption at each desorption curve shifted to a slightly higher temperature as the heating rate increased. However, the TDS spectra obtained at various heating rates show that the absorption of H_2 and D_2 is identical (Table S2). The desorption energy of MSC-30 was calculated using Equations (8) and (9). The H_2 and D_2 desorption energies of MSC-30 were obtained using Equations (8) and (9), as shown in Figure 6c,d, respectively. The desorption energies of hydrogen and deuterium calculated by Equation (8) were 3.15 and 3.95 kJ mol^{-1}, and the desorption energies of H_2 and D_2 using Equation (9) were 3.40 and 3.94 kJ mol^{-1}. D_2 has a higher desorption energy than H_2 by the KQS effect, resulting in high D_2 uptake. These values fall within the typical energy range reported for hydrogen adsorption in microporous carbons. Previous studies on activated carbons and related nanoporous carbons generally report adsorption enthalpies for H2 in the range of ~4–9 kJ mol^{-1} depending on pore size and surface chemistry [47, 48]. The slightly lower values obtained for MSC-30 are therefore consistent with weak physisorption in high-surface-area carbons with relatively large micropores, where adsorption is dominated by dispersive interactions rather than specific binding sites. Importantly, the systematic increase in Edes from H_2 to D_2 observed here is consistent with the zero-point-energy difference underlying quantum sieving, which leads to stronger effective confinement of the heavier isotope in nanoporous carbons.

5 | Conclusion

We developed an advanced cryogenic TDS (AC-TDS) platform that quantifies H_2, D_2, and HD over an unprecedented 15–900 K window, unifying cryogenic physisorption and high-temperature chemisorption analysis in a single instrument. By coupling a thermally decouplable bellows stage with rigorously validated calibrants (TiH_2 and $Pd_{95}Ce_5$), the system delivers absolute isotope doses and responses, enabling reproducible, cross-temperature quantification. Protocols that contrast room-temperature vs. liquefaction-temperature gas dosing provide a simple diagnostic to distinguish rigid from flexible frameworks and to pinpoint temperature-dependent gate-opening/closure. Using binary and ternary isotope gas mixtures, the platform directly resolves isotope-dependent uptake, including robust HD quantification, and extracts desorption energetics from variable-ramp measurements, revealing stronger D_2 binding consistent with quantum sieving. Together, these capabilities establish AC-TDS as a practical, low-sample-mass toolkit for mapping site energetics, pore accessibility, and isotope selectivity in porous solids. We anticipate that the methodology will accelerate materials discovery and mechanism-driven optimization for hydrogen-isotope separations (and storage), and is readily extensible to in situ/operando coupling with diffraction or spectroscopy and to microkinetic modeling of device-scale processes.

Acknowledgements

This research was funded by the National Research Foundation of Korea (NRF), Government of Korea (MSI) (RS-2022-NR070566: RS-2025-16063688: RS-2026-25498508: RS-2025-02982993).

Conflicts of Interest

None of the authors have a conflict of interest to disclose.

Data Availability Statement

The data that support the findings of this study are available from the corresponding author upon reasonable request.

References

1. P. Schah-Mohammedi, I. G. Shenderovich, C. Detering, et al., "Hydrogen/Deuterium-Isotope Effects on NMR Chemical Shifts and Symmetry of Homoconjugated Hydrogen-Bonded Ions in Polar Solution," *Journal of the American Chemical Society* 122, no. 51 (2000): 12878–12879, https://doi.org/10.1021/ja0017615.

2. H. Benedict, C. Hoelger, F. Aguilar-Parrilla, et al., "Hydrogen/Deuterium Isotope Effects on the ^{15}N NMR Chemical Shifts and Geometries of Low-Barrier Hydrogen Bonds in the Solid State," *Journal of Molecular Structure* 378, no. 1 (1996): 11–16, https://doi.org/10.1016/0022-2860(95)09143-2.

3. F. Wehrmann, J. Albrecht, E. Gedat, et al., "Hydrogen Deuterium Isotope Effect on Exchange Rates in η^2 Bond Transition Metal Dihydrogen Complexes Revealed by ^2H Solid State NMR Spectroscopy," *The Journal of Physical Chemistry A* 106, no. 12 (2002): 2855–2861, https://doi.org/10.1021/jp012087w.

4. J. F. Ankner, W. T. Heller, K. W. Herwig, F. Meilleur, and D. A. Myles, "Neutron Scattering Techniques and Applications in Structural Biology," *Current Protocols in Protein Science* 72, no. 1 (2013): 17.16.1–17.16.34, https://doi.org/10.1002/0471140864.ps1716s72.

5. G. C. Reichart, R. A. Register, W. W. Graessley, R. Krishnamoorti, and D. J. Lohse, "Effect of Nonuniform Deuterium Labeling on Small-Angle Neutron Scattering Results for Polymer Blends," *Macromolecules* 28, no. 26 (1995): 8862–8864, https://doi.org/10.1021/ma00130a021.

6. K. Cheng, J. Lee, and J. W. Lyding, "Approach to Enhance Deuterium Incorporation for Improved Hot Carrier Reliability in Metal-Oxide-Semiconductor Devices," *Applied Physics Letters* 77, no. 15 (2000): 2358–2360, https://doi.org/10.1063/1.1317546.

7. J. W. Lyding, K. Hess, and I. C. Kizilyalli, "Reduction of Hot Electron Degradation in Metal Oxide Semiconductor Transistors by Deuterium Processing," *Applied Physics Letters* 68, no. 18 (1996): 2526–2528, https://doi.org/10.1063/1.116172.

8. J. Atzrodt, V. Derdau, W. J. Kerr, and M. Reid, "C−H Functionalisation for Hydrogen Isotope Exchange,", *Angewandte Chemie International Edition* 57, no. 12, (2017): 1–26.

9. T. G. Gant, "Using Deuterium in Drug Discovery: Leaving the Label in the Drug," *Journal of Medicinal Chemistry* 57, no. 9 (2014): 3595–3611, https://doi.org/10.1021/jm4007998.

10. T. E. Sharp and H. S. Johnston, "Hydrogen—Deuterium Kinetic Isotope Effect, an Experimental and Theoretical Study Over a Wide

Range of Temperature," *The Journal of Chemical Physics* 37, no. 7 (1962): 1541–1553, https://doi.org/10.1063/1.1733321.

11. B. Leyh, "Ion Dissociation Kinetics in Mass Spectrometry", *Encyclopedia of Spectroscopy and Spectrometry (Second Edition); Lindon, J. C., Ed.; Academic Press: Oxford*, (1999) pp 1127–1134, https://doi.org/10.1016/B978-0-12-374413-5.00178-0.

12. J. F. Meagher, P. Kim, J. Lee, and R. B. Timmons, "Kinetic Isotope Effects in the Reactions of Hydrogen and Deuterium Atoms with Dimethyl Ether and Methanol," *The Journal of Physical Chemistry* 78, no. 26 (1974): 2650–2657, https://doi.org/10.1021/j100619a003.

13. N. N. Greenwood and A. Earnshaw, *Chemistry of the Elements* (Elsevier, 2012).

14. H. K. Rae, *Separation of Hydrogen Isotopes* (ACS Publications, 1978).

15. J. Y. Kim, H. Oh, and H. R. Moon, "Hydrogen Isotope Separation in Confined Nanospaces: Carbons, Zeolites, Metal–Organic Frameworks, and Covalent Organic Frameworks," *Advanced Materials* 31, no. 20 (2019): 1805293, https://doi.org/10.1002/adma.201805293.

16. R. Muhammad, S. Kim, J. Park, et al., "Chemical Affinity-Assisted H_2 Isotope Separation Using Ca-Rich Onion-Peel-Derived Nanoporous Carbon Composite," *Materials Chemistry Frontiers* 5, no. 22 (2021): 8018–8024, https://doi.org/10.1039/D1QM00894C.

17. H. Kim, S. Jee, J. Park, et al., "High D_2/H_2 Selectivity Performance in MOF-303 Under Ambient Pressure for Potential Industrial Applications," *Separation and Purification Technology* 325 (2023): 124660, https://doi.org/10.1016/j.seppur.2023.124660.

18. Q. Yan, J. Wang, L. Zhang, et al., "A Squarate-Pillared Titanium Oxide Quantum Sieve Towards Practical Hydrogen Isotope Separation," *Nature Communications* 14, no. 1 (2023): 4189, https://doi.org/10.1038/s41467-023-39871-x.

19. M. Liu, L. Zhang, M. A. Little, et al., "Barely Porous Organic Cages for Hydrogen Isotope Separation," *Science* 366, no. 6465 (2019): 613–620, https://doi.org/10.1126/science.aax7427.

20. J. Ha, M. Jung, J. Park, H. Oh, and H. R. Moon, "Thermodynamic Separation of Hydrogen Isotopes Using Hofmann-Type Metal–Organic Frameworks with High-Density Open Metal Sites," *ACS Applied Materials & Interfaces* 14, no. 27 (2022): 30946–30951, https://doi.org/10.1021/acsami.2c07829.

21. L. Zhang, S. Jee, J. Park, et al., "Exploiting Dynamic Opening of Apertures in a Partially Fluorinated MOF for Enhancing H_2 Desorption Temperature and Isotope Separation," *Journal of the American Chemical Society* 141, no. 50 (2019): 19850–19858, https://doi.org/10.1021/jacs.9b10268.

22. N. F. Cessford, N. A. Seaton, and T. Düren, "Evaluation of Ideal Adsorbed Solution Theory as a Tool for the Design of Metal–Organic Framework Materials," *Industrial & Engineering Chemistry Research* 51, no. 13 (2012): 4911–4921, https://doi.org/10.1021/ie202219w.

23. C.-W. Wu and S. Sircar, "Comments on Binary and Ternary Gas Adsorption Selectivity," *Separation and Purification Technology* 170 (2016): 453–461, https://doi.org/10.1016/j.seppur.2016.06.053.

24. S.-Y. Jung, D. Park, S. Kim, and H. Oh, "Comprehensive Design and Experimental Protocol for Scalable and Temperature-Controllable Cryogenic Hydrogen Isotope Separation," *Analytical Chemistry* 96, no. 51 (2024): 20277–20286, https://doi.org/10.1021/acs.analchem.4c04956.

25. Z. Junbo, G. Liping, and W. Kuisheng, "Hydrogen Isotope Separation by Cryogenic Gas Chromatography Using the Combined Column of 5Åmolecular Sieve and Al_2O_3," *International Journal of Hydrogen Energy* 31, no. 14 (2006): 2131–2135, https://doi.org/10.1016/j.ijhydene.2006.02.002.

26. M. Li, Z. Wang, Y. An, et al., "Cryogenic Gas Chromatographic Separation of Hydrogen Isotopes Using Pillared-Layer MOFs Composites as Stationary Phase," *International Journal of Hydrogen Energy* 47, no. 1 (2022): 339–347, https://doi.org/10.1016/j.ijhydene.2021.10.039.

27. M. Haluska, M. Hirscher, M. Becher, U. Dettlaff-Weglikowska, X. Chen, and S. Roth, "Interaction of Hydrogen Isotopes with Carbon Nanostructures," *Materials Science and Engineering: B* 108, no. 1-2 (2004): 130–133, https://doi.org/10.1016/j.mseb.2003.10.092.

28. D. Collins and W. Spicer, "The Adsorption of CO, O_2, and H_2 on Pt: I. Thermal Desorption Spectroscopy Studies," *Surface Science* 69, no. 1 (1977): 85–113, https://doi.org/10.1016/0039-6028(77)90163-7.

29. Y. Men, H. Gnaser, C. Ziegler, R. Zapf, V. Hessel, and G. Kolb, "Characterization of $Cu/CeO_2/\gamma$-Al_2O_3 Thin Film Catalysts by Thermal Desorption Spectroscopy," *Catalysis Letters* 105 (2005): 35–40, https://doi.org/10.1007/s10562-005-8002-4.

30. S. Frappart, A. Oudriss, X. Feaugas, et al., "Hydrogen Trapping in Martensitic Steel Investigated Using Electrochemical Permeation and Thermal Desorption Spectroscopy," *Scripta Materialia* 65, no. 10 (2011): 859–862, https://doi.org/10.1016/j.scriptamat.2011.07.042.

31. J. Wang, S. Funk, and U. Burghaus, "Adsorption Dynamics of CO_2 on Copper-Precovered ZnO (0001)–Zn: A Molecular-Beam Scattering and Thermal-Desorption Spectroscopy Study," *The Journal of Chemical Physics* 123, no. 22 (2005): 204710.

32. F. von Zeppelin, M. Haluška, and M. Hirscher, "Thermal Desorption Spectroscopy as a Quantitative Tool to Determine the Hydrogen Content in Solids," *Thermochimica Acta* 404, no. 1-2 (2003): 251–258, https://doi.org/10.1016/S0040-6031(03)00183-7.

33. D. Cao, S. Peng, X. Chen, et al., "Analysis of Hydrogen Isotopes with Quadrupole Mass Spectrometry," *Analytical Methods* 9, no. 20 (2017): 3067–3072, https://doi.org/10.1039/C7AY00457E.

34. B. Panella, M. Hirscher, and B. Ludescher, "Low-Temperature Thermal-Desorption Mass Spectroscopy Applied to Investigate the Hydrogen Adsorption on Porous Materials," *Microporous and Mesoporous Materials* 103, no. 1–3 (2007): 230–234, https://doi.org/10.1016/j.micromeso.2007.02.001.

35. H. Oh, N. Tumanov, V. Ban, et al., "Small-Pore Hydridic Frameworks Store Densely Packed Hydrogen," *Nature Chemistry* 16, no. 5 (2024): 809–816, https://doi.org/10.1038/s41557-024-01443-x.

36. W. Cai, T. Lee, M. Lee, et al., "Thermal Structural Transitions and Carbon Dioxide Adsorption Properties of Zeolitic Imidazolate Framework-7 (ZIF-7)," *Journal of the American Chemical Society* 136, no. 22 (2014): 7961–7971, https://doi.org/10.1021/ja5016298.

37. R. Xiong, R. Balderas-Xicohténcatl, L. Zhang, et al., "Thermodynamics, Kinetics and Selectivity of H_2 and D_2 on Zeolite 5A Below 77K," *Microporous and Mesoporous Materials* 264 (2018): 22–27, https://doi.org/10.1016/j.micromeso.2017.12.035.

38. M. Ege, W. Ulfert, and H. Kronmüller, "Diatomic Hydrogen-Metal Complexes in Dilute Palladium-Rare Earth Alloys," *Le Journal de Physique IV* 6 (1996): C8–43, https://doi.org/10.1051/jp4:1996807.

39. M. Ege and H. Kronmüller, "Mechanical Relaxation Processes of Hydrogen in Dilute Palladium-Rare Earth Alloys," *Journal of Alloys and Compounds* 261, no. 1-2 (1997): 231–241, https://doi.org/10.1016/S0925-8388(97)00219-3.

40. B. Coluzzi, A. Biscarini, R. Campanella, et al., "Reorientation of the Ce–D Pairs in a $Pd_{95}Ce_5D_n$ Alloy," *Journal of Alloys and Compounds* 253-254 (1997): 360–363, https://doi.org/10.1016/S0925-8388(96)03043-5.

41. L. Zhang, *Experimental Investigation on Hydrogen Isotope Separation in Nanoporous Materials* (Universität Stuttgart, 2020).

42. T. W. Kim, M. Kim, S. K. Kim, et al., "Remarkably Fast Low-Temperature Hydrogen Storage Into Aromatic Benzyltoluenes Over MgO-Supported Ru Nanoparticles with Homolytic and Heterolytic H_2 Adsorption," *Applied Catalysis B: Environmental* 286 (2021): 119889, https://doi.org/10.1016/j.apcatb.2021.119889.

43. J. Y. Kim, R. Balderas-Xicohténcatl, L. Zhang, et al., "Exploiting Diffusion Barrier and Chemical Affinity of Metal–Organic Frameworks for Efficient Hydrogen Isotope Separation," *Journal of the American*

Chemical Society 139, no. 42 (2017): 15135–15141, https://doi.org/10.1021/jacs.7b07925.

44. B. Panella, K. Hönes, U. Müller, et al., "Desorption Studies of Hydrogen in Metal–Organic Frameworks," *Angewandte Chemie International Edition* 47, no. 11 (2008): 2138–2142, https://doi.org/10.1002/anie.200704053.

45. D. A. King, "Thermal Desorption from Metal Surfaces: A Review," *Surface Science* 47, no. 1 (1975): 384–402, https://doi.org/10.1016/0039-6028(75)90302-7.

46. J.-L. Falconer and R. Madix, "Flash Desorption Activation Energies: DCOOH Decomposition and CO Desorption from Ni (110)," *Surface Science* 48, no. 2 (1975): 393–405, https://doi.org/10.1016/0039-6028(75)90414-8.

47. G. Sdanghi, S. Schaefer, G. Maranzana, A. Celzard, and V. Fierro, "Application of the Modified Dubinin-Astakhov Equation for a Better Understanding of High-Pressure Hydrogen Adsorption on Activated Carbons," *International Journal of Hydrogen Energy* 45, no. 48 (2020): 25912–25926, https://doi.org/10.1016/j.ijhydene.2019.09.240.

48. S. K. Bhatia and A. L. Myers, "Optimum conditions for Adsorptive Storage," *Langmuir* 22, no. 4 (2006): 1688–1700.

Supporting Information

Additional supporting information can be found online in the Supporting Information section.

Supporting File: smll73657-sup-0001-SuppMat.docx.